Acta Cryst. (1997). **B53**, 420–428

Synchrotron X-ray Studies of $LiNbO_3$ and $LiTaO_3$

R. HSU,[a]* E. N. MASLEN,[a]† D. DU BOULAY[a] AND N. ISHIZAWA[b]

[a]*Crystallography Centre, University of Western Australia, Nedlands 6009, Australia, and* [b]*Research Laboratory of Engineering Materials, Tokyo Institute of Technology, 4259 Nagatsuta, Midori-Ku, Yokohama 227, Japan. E-mail: rhsu@mail.ncku.edu.tw*

(*Received 18 July 1995; accepted 13 February 1997*)

Abstract

The structural geometry, vibrations and deformation density $\Delta\rho$ for lithium niobate, $LiNbO_3$, and lithium tantalate, $LiTaO_3$, are derived from synchrotron radiation diffraction measurements. Electron density is transferred from the Nb (Ta) atom towards the large O_3 triangle near the Li atom. Spontaneous polarizations of 0.43 ($LiNbO_3$) and 0.33 cm^{-2} ($LiTaO_3$), calculated with Hirshfeld charges, agree qualitatively with experimental values of 0.71 and 0.50 cm^{-2}, respectively. Both strong Li···Nb (Ta) interactions in the structure are markedly shorter than all Li···Li, Nb···Nb or Ta···Ta vectors, as expected if the Li and Nb (Ta) cations carry charges of opposite sign. The Li atom's negative charge plays a pivotal role in the polarization responsible for ferroelectricity. $LiNbO_3$, space group $R3c$, rhombohedral, M_r = 147.8, a = 5.493 (2) Å, α = 55.89 (3)°, V = 106.02 (4) Å^3, Z = 2, D_x = 4.629 Mg m^{-3}, $F(000)$ = 136, μ(0.7 Å) = 5.01 mm^{-1}, y_{min} = 0.27, T = 293 K, R = 0.015, wR = 0.015, S = 3.276 (84) for 773 unique reflections. $LiTaO_3$, $R3c$, rhombohedral, M_r = 235.9, a = 5.471 (2) Å, α = 56.16 (3)°, V = 105.51 (4) Å^3, Z = 2, D_x = 7.412 Mg m^{-3}, $F(000)$ = 200, μ(0.7 Å) = 50.03 mm^{-1}, y_{min} = 0.32, T = 293 K, R = 0.016, wR = 0.022, S = 1.372 (35) for 773 unique reflections.

1. Introduction

Lattice dynamics (Cochran, 1973) and statistical theory (Lines & Glass, 1979) provide some insight into ferroelectricity, but a fully predicative theory has yet to emerge (Kittel, 1986). The relationship of ferroelectricity to crystal structure (Abrahams & Keve, 1971) was reviewed by Abrahams (1994). Accurate imaging of the deformation density for archetypal ferroelectric compounds may help to clarify those aspects that are not yet fully understood.

A huge number of publications (Abrahams & Marsh, 1986) reviewed by Prokhorov & Kuz'minov (1990) indicates high interest in the ferroelectricity of $LiNbO_3$. Its room-temperature structure, studied by single-crystal X-ray diffraction (Abrahams, Reddy & Bernstein, 1966) and neutron diffraction (Abrahams, Hamilton & Reddy, 1966), is closely related to those of corundum and ilmenite (Megaw, 1973). The isomorphous compound $LiTaO_3$, studied using single-crystal X-ray (Abrahams & Bernstein, 1967) and neutron diffraction (Abrahams, Hamilton & Sequeira, 1967), is a test-case displacement ferroelectric (Lines, 1969). Both $LiNbO_3$ and $LiTaO_3$ are frozen ferroelectrics (Megaw, 1954), with polarities retained by structural forces too large to be overcome by normal fields. Their behaviour under electric, elastic and magnetic fields has been studied extensively (*e.g.* Ståhl, Kvick & Abrahams, 1990). Anharmonic motion and residual electron density in $LiNbO_3$ and $LiTaO_3$ were studied by Ohgaki, Tanaka & Marumo (1989, 1992). Anharmonicity at room temperature is stronger in $LiTaO_3$ than in $LiNbO_3$, which has a higher phase transition (Curie) temperature T_c (Cochran, 1973).

The second-order transition is a decrease in crystal symmetry with no abrupt discontinuity. The paraelectric space group for $LiNbO_3$ above T_c was identified as $R\bar{3}$ by polycrystal X-ray diffraction (Abrahams, Levinstein & Reddy, 1966), but as $R\bar{3}c$ by neutron powder diffraction (Boysen & Altorfer, 1994). The Nb atom in the non-polar paraelectric phase is midway between adjoining O layers, with Li in an O-atom layer $c/4$ from the Nb atom. Boysen & Altorfer (1994) describe the $LiNbO_3$ phase transition as between two models, but it can be represented in terms of a fixed O-atom framework (Abrahams, Levinstein & Reddy, 1966), whether or not the glide plane is replaced by a threefold inversion.

The phase transition has been described in terms of the dynamics of low-frequency (soft) optical phonons. A soft mode for a displacive transition can propagate through a crystal. For a merely diffusive soft mode there is no real phonon, but only large amplitude hopping between wells (Kittel, 1986). Study of the $LiNbO_3$ phase transition was extended to polarity reversal by postulating a transition from the ferroelectric structure through the paraelectric state to the original structure with polarity reversed (Megaw, 1954; Abrahams, Levinstein & Reddy, 1966), which is identical except for a change of sign in the relative coordinates (Abrahams, 1994).

2. Experimental

$LiNbO_3$ ($LiTaO_3$) crystals, prepared by flux growth (Hsu, 1995), had sharp edges, well faceted reflec-

† Deceased 3rd February 1997.

Table 1. *Experimental details*

	$LiNbO_3$	$LiTaO_3$
Crystal data		
Chemical formula	$LiNbO_3$	$LiTaO_3$
Chemical formula weight	147.8	235.9
Cell setting	Trigonal	Trigonal
Space group	*R*3*c*	*R*3*c*
a (Å)	5.148 (3)	5.154 (3)
b (Å)	5.148 (3)	5.154 (3)
c (Å)	13.863 (3)	13.783 (3)
α (°)	90.000 (10)	90.000 (10)
V (Å^3)	318.2 (4)	317.1 (4)
Z	6	6
D_x (Mg m^{-3})	4.629	7.412
Radiation type	X-ray wiggler	X-ray wiggler
Wavelength (Å)	0.7	0.7
No. of reflections for cell parameters	6	6
θ range (°)	41.273–41.288	41.283–41.288
μ (mm^{-1})	5.01	50.03
Temperature (K)	293	293
Crystal form	Rectangular	Rectangular
Crystal size (mm)	0.1400 (3) × 0.0770 (3) × 0.0500 (3)	0.0470 (3) × 0.0360 (3) × 0.0228 (3)
Crystal colour	Transparent	Transparent
Data collection		
Diffractometer	Tsukuba	Tsukuba
Data collection method	$\omega/2\theta$ scans	$\omega/2\theta$ scans
Absorption correction	Analytical	Analytical
T_{min}	0.65	0.1560
T_{max}	0.79	0.3676
No. of measured reflections	4622	4622
No. of independent reflections	773	773
No. of observed reflections	773	773
Criterion for observed reflections	$F > 0.0001\sigma(F)$	$F > 0.0001\sigma(F)$
R_{int}	0.0399	0.0598
θ_{max} (°)	50.0	50.0
Range of h, k, l	$-11 \rightarrow h \rightarrow 11$	$-11 \rightarrow h \rightarrow 11$
	$-11 \rightarrow k \rightarrow 11$	$-11 \rightarrow k \rightarrow 11$
	$-11 \rightarrow l \rightarrow 11$	$-11 \rightarrow l \rightarrow 11$
No. of standard reflections	6	6
Frequency of standard reflections	Every 100 reflections	Every 100 reflections
Intensity decay (%)	3.9	16
Refinement		
Refinement on	*F*	*F*
R	0.015	0.016
wR	0.015	0.022
S	3.276	1.372
No. of reflections used in refinement	773	773
No. of parameters used	16	16
H-atom treatment	H-atom parameters not refined	H-atom parameters not refined
Weighting scheme	σ	σ
$(\Delta/\sigma)_{max}$	0.00001	0.00001
$\Delta\rho_{max}$ (e Å^{-3})	3.50	3.35
$\Delta\rho_{min}$ (e Å^{-3})	−2.684	−5.946
Extinction method	Zachariasen (1967)	Zachariasen (1967)
Extinction coefficient	20 194 (400)	5815 (180)
Source of atomic scattering factors	*International Tables for X-ray Crystallography* (1974, Vol IV, Tables 2.2B and 2.3.1)	*International Tables for X-ray Crystallography* (1974, Vol IV, Tables 2.2B and 2.3.1)
Absolute configuration	None	None
Computer programs		
Data reduction	*Xtal DIFDAT SORTRF ABSORB ADDREF* (Hall, Flack & Stewart, 1992)	*Xtal DIFDAT SORTRF ABSORB ADDREF* (Hall, Flack & Stewart, 1992)
Structure solution	*Xtal* (Hall, Flack & Stewart, 1992)	*Xtal* (Hall, Flack & Stewart, 1992)
Structure refinement	*Xtal CRYLSQ* (Hall, Flack & Stewart, 1992)	*Xtal CRYLSQ* (Hall, Flack & Stewart, 1992)
Preparation of material for publication	*Xtal CIFIO* (Hall, Flack & Stewart, 1992)	*Xtal CIFIO* (Hall, Flack & Stewart, 1992)

tive {011}, {101} and {110} faces and dimensions 0.14 × 0.05 × 0.077 (0.0228 × 0.047 × 0.036) mm, accurate to 0.3 mm, measured and indexed using optical and scanning electron Philips SEM505 microscopes. Intensity data, measured with 0.7 Å X-radiation on the BL14A four-circle diffractometer (Satow & Iitaka, 1989) at the Tsukuba Photon Factory. The 20 keV critical energy wiggler is polarized vertically with polarization ratio 0.95. The beam optics comprise a double-crystal Si(111) monochromator with 2θ angle 12.818° and a double-focusing fused quartz mirror coated with Pt, adjusted to yield such high flux that, even for small

crystals, dead time loss for the strongest reflections causes double-peaked profiles by drastically reducing intensity near the peak centre. An 80 μm copper foil with attenuation factor 26.465 was inserted when the peak count rate exceeded the linear range of 20 000 counts s^{-1} for the NaI scintillation counter. Lattice constants in the rhombohedral setting were determined from ±800, ±080 and ±008 reflections at $2\theta \simeq 82.5°$. Intensities were measured for 4622 reflections in a reciprocal space sphere with $\theta \le 50°$, $11 \le h \le 11$, $11 \le k \le 11$, $11 \le l \le 11$, using $\omega/2\theta$ scans at 16° min^{-1}, reducing to 773 unique reflections by averaging equivalents.* Peak scan widths $A + B \tan\theta$ with $A = 0.25$ (0.3), $B = 0.05$ (0.2)°. The incident beam stability monitored every 100 reflections with six standard reflections ±800, ±080, ±008; maximum variation 3.9 (16)%. 15 blind-region-affected reflections were excluded from the $LiNbO_3$ data, along with 41 (24) apparently significant but anomalous values, identified as Renninger reflections. The Renninger effect for $LiTaO_3$ was mild compared with that for $LiNbO_3$, as expected from the crystal volumes.

Absorption corrections (Alcock, 1974), evaluated analytically with the linear absorption coefficient $\mu(0.7\ Å)$ = 5.01 (50.03) mm^{-1}, were calculated from *International Tables for X-ray Crystallography* (1968, Vol. III). The corrections within the range 1.27–1.54 (2.72–6.41) reduced $R_{int}(I)$ from 0.047 (0.129) to 0.040 (0.060). Dispersion corrections: $\Delta f'$, $\Delta f''$ 0.0003, 0.0001 for Li; 0.0103, 0.0059 for O; 1.9958, 0.7586 for Nb; 0.6853, 6.3915 for Ta (Creagh, 1992). All subsequent calculations used the *Xtal*3.2 system of programs (Hall, Flack & Stewart, 1992) on Sun Sparc and DEC 5000/120 workstations.

Extinction, being a consequence of multiple diffraction, was expected to be as significant for the strong reflections as was the Renninger effect for weak reflections. Corrections based on equivalent reflection intensities (Maslen & Spadaccini, 1993) were unsatisfactory, as irregular mesostructures for the flux grown $LiNbO_3$ and $LiTaO_3$ crystals cause unpredictable differences even between Friedel-related strong reflections. The robust though biased Zachariasen (1967) formalism, as implemented by Larson (1970), yielded y_{min} = 0.27 (0.32) for the $0\bar{1}\bar{1}2$ reflection, its severity justifying reservations about the Zachariasen formalism. The sensitivity of the atomic charges to extinction was tested by adjusting the isotropic extinction parameter g by a standard deviation. While not changing the refinement indices appreciably, the Hirshfeld charges changed by one standard deviation, tentatively indicating adequacy of the Zachariasen correction. Higher weight was given to the consistency between the two analyses.

* Lists of anisotropic displacement parameters, Renninger-affected and blind-region-affected reflections, and structure factors have been deposited with the IUCr (Reference: AS0700). Copies may be obtained through The Managing Editor, International Union of Crystallography, 5 Abbey Square, Chester CH1 2HU, England.

Table 2. *Fractional atomic coordinates and equivalent isotropic displacement parameters (Å²)*

$$U_{eq} = (1/3)\sum_i\sum_j U^{ij} a_i^* a_j^* \mathbf{a}_i.\mathbf{a}_j.$$

	x	y	z	U_{eq}
$LiNbO_3$				
Li	0.00000	0.00000	0.2806 (4)	0.0136 (16)
Nb	0.00000	0.00000	−0.0010 (2)	0.00435 (4)
O	0.04751 (5)	0.34301 (5)	0.0625 (5)	0.00669 (6)
$LiTaO_3$				
Li	0.00000	0.00000	0.2808 (16)	0.017 (7)
Ta	0.00000	0.00000	0.0009 (8)	0.00354 (5)
O	0.04947 (11)	0.34337 (11)	0.0698 (18)	0.00614 (12)

The structure was refined using hexagonal axes. 16 independent parameters, including the extinction parameter r^*, were determined by full-matrix least-squares refined to convergence (shift/σ < 0.00001), minimizing $\sum w_i(|F_o| - |F_c|)^2$ with w_i equal to $1/\sigma^2(F_o)$ for all measured structure factors. The stronger reflections affected acutely by extinction, thus weighted, dominate the residual. Refinement indices R = 0.052 (0.039), wR = 0.058 (0.058), S = 13.0 (3) [3.60 (9)] reduced to R = 0.015 (0.016), wR = 0.015 (0.022), S = 3.28 (8) [1.37 (4)], by the extinction correction. Refined atomic coordinates and isotropic displacement parameters are listed in Table 2. Maximum height in final difference map $\Delta\rho_{max}$ = 3.5 (3) [3.4 (6)] e $Å^{-3}$ and minimum height $\Delta\rho_{min}$ = 2.7 (3) [6.0 (6)] e $Å^{-3}$.

The full-matrix least-squares error surface for the $LiTaO_3$ refinement had two closely spaced minima. Refinement indices for the incorrect structure were R = 0.017, wR = 0.023 and S = 1.43 (4). The structure model for what is perceived to be the subsidiary minimum is very close to that in Table 1. The double minimum in the least-squares refinement originates in a strong correlation (Lipson & Cochran, 1957) of the vibration tensor with the bonding redistribution for the Ta-atom electrons.

3. Structural geometry

The O anion and cation sublattices interpenetrate. Six equidistant O layers per c axis (Megaw, 1968) are in an anticlockwise–clockwise sequence (Megaw, 1973) with B-occupied, vacant and Li-occupied octahedral interstices, where B denotes Nb (Ta). The four-cation sequence $B\cdots$vacancy$\cdots$Li$\cdots B\cdots$vacancy$\cdots$Li$\cdots B$, spaced non-uniformly along **c**, has one O layer in the second and fourth zones. Two O layers are interposed between the Li$\cdots B$-atom pairs delineating the first and third zones (Abrahams, Reddy & Bernstein, 1966; Abrahams & Bernstein, 1967).

Interatomic distances are listed in Table 3. There is one O_3 equilateral triangle of side 2.870 (2) [2.870 (2)] Å between the B atom and the cavity, another of side 3.354 (2) [3.373 (2)] Å between the cavity and Li, and a third with side 2.733 (2) [2.727 (2)] Å between the Li

Table 3. *Selected interaction-vector lengths (Å) and O—M—O′ (°) angles*

		$LiNbO_3$		$LiTaO_3$	
Coordination		*M*—O		*M*—O	
Li	12	Li—O	2.063 (3) × 3		2.041 (10) × 3
		Li—O	2.245 (6) × 3		2.31 (2) × 3
		Li—O	3.291 (2) × 3		3.265 (7) × 3
		Li—O	3.449 (8) × 3		3.35 (3) × 3
B	6	Nb—O	1.876 (4) × 3	Ta—O	1.910 (14) × 3
		Nb—O	2.130 (5) × 3	Ta—O	2.072 (18) × 3
M—*M* contacts					
	Li	Nb		Li	Ta
Li	3.765 (5) × 2	3.028 (6)		3.76 (2) × 2	3.03 (2)
		3.058 (2)			3.065 (6)
		3.372 (3)			3.360 (12)
		3.904 (6)			3.86 (2)
B		3.765 (3) × 2			3.759 (10) × 2
O—O contacts					
		O			O
O		2.733 (2) × 2			2.727 (2) × 2
		2.804 (8) × 2			2.79 (3) × 2
		2.838 (8) × 2			2.83 (3) × 2
		2.870 (2) × 2			2.870 (2) × 2
		3.038 (8) × 2			3.04 (3) × 2
		3.354 (2) × 2			3.373 (2) × 2
O—*M*—O				O—*M*—O	
O—Li—O		108.7 (2)			111.4 (7)
O—Li—O		75.0 (2)			72.5 (8)
O—Li—O		81.1 (2)			79.6 (7)
O—Li—O		89.6 (2)			88.4 (6)
O—Li—O		154.2 (3)			149.8 (12)
O—Nb—O		99.8 (2)		O—Ta—O	97.4 (7)
O—Nb—O		79.8 (2)		O—Ta—O	82.3 (7)
O—Nb—O		88.6 (2)		O—Ta—O	88.9 (6)
O—Nb—O		90.0 (2)		O—Ta—O	90.4 (6)
O—Nb—O		165.7 (3)		O—Ta—O	169.2 (10)

and *B* atoms. The shortest *B*—O and Li—O bonds link to the larger O_3 triangle in each case.

By analogy with the ideal ABO_3 perovskite structure, the Li atom has 12 O-atom neighbours, shown for $LiNbO_3$ in Fig. 1(*a*). The three longest of the 12 Li—O vectors link to the O_3 triangular face common to the BO_6 and the empty O_6 octahedra. The remaining three Li—O vectors link to three O atoms coplanar with those linked by the shortest Li—O bonds.

Both the LiO_{12} and BO_6 polyhedra are asymmetric (Fig. 1). The *B* atom is 0.25 (4) [0.20 (4)] Å from the mid-point between the oxygen layers. The Li atom is 0.73 (1) [0.60 (2)] Å in the **c** direction from the double oxygen layers. Displacive Δz vectors for the Li and *B* nuclei defined thus are parallel.

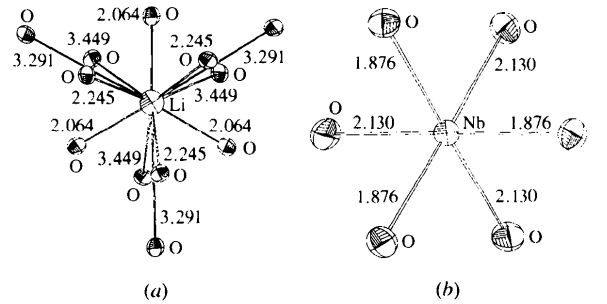

(*a*) (*b*)

Fig. 1. Coordination polyhedra for (*a*) Li and (*b*) Nb in $LiNbO_3$. Vibration ellipsoids at 90% probability.

Attractive Coulomb potentials between 'free' *B* and O ions with rigid ion radii would hold the *B* cations symmetrically in the BO_6 octahedron, but the BO_6 structural geometry is strongly asymmetric. The asymmetric Nb (Ta) environment cannot be explained in terms of that atom's electron valence states as the *s* and *d* character of the atom's valence states also favour symmetric geometry. The idealized valence orbital picture is perturbed by the Li···*B* interactions. The Li···*B* distance spanning two layers increases from 3.028 (6) to 3.904 (6) [3.03 (2) to 3.86 (2)] Å. There are three Li···*B* vectors shorter than all Li···Li or *B*···*B* vectors.

4. Atomic vibrations

The Li and *B* atoms on the triad axis undergo isotropic motion in the *xy* plane (Ohgaki, Tanaka & Marumo, 1989). The Li atom's large U^{ii} values indicate that it is packed loosely. Whereas the Li vibration is larger in $LiTaO_3$, the Ta- and O-atom vibrations are smaller than those for the Nb and O atoms in $LiNbO_3$. Whereas the *B*-atom vibration amplitude is a minimum in the *c* direction, the Li vibration maximizes along **c**.

For the three O-defined octahedra in $LiNb(Ta)O_3$, rigid-body TLS (translation, libration and screw) tensors (Schomaker & Trueblood, 1968) were evaluated using the *RIGBY* (Varghese, 1972) program with the constraint trace (**S**) = 0. The $R_{rbv} = \sum|U^{ij}_{obs} - U^{ij}_{calc}|/\sum U^{ij}_{obs}$ value of 0.090 (0.119) that minimizes $\sum(U^{ij}_{obs} - U^{ij}_{calc})^2$ for the anisotropic vibrations allows the BO_6 octahedra in both $LiNbO_3$ and $LiTaO_3$ to be regarded as rigid, with O atoms tightly bound along all *B*—O bonds. The *B*—O bond covalence implied favours $(\uparrow\downarrow - \downarrow\uparrow)/2^{1/2}$ spin configurations for the valence electron pairs. The r.m.s libration amplitudes about orthonormal *x*, *y* and *z* axes for the BO_6 octahedron are 1.9, 1.9 and 1.1 (1.9, 1.9 and 1.4)°, respectively.

In contrast to the BO_6 group, a rigid-body model for the LiO_6 octahedron is inappropriate because of weaker Li—O bonding. Vibrations for the vacant O_6 octahedron are larger than those for BO_6, but smaller than those for the LiO_6 group. Neither librations nor screw motions are significant, as expected for a structural unit lacking a central atom to attract O ligands.

The O—Li—O angle between two of the shortest Li—O bonds is 108.7 (111.4)° compared with 90° for an ideal octahedron or 88.6 (88.9)° for the corresponding BO_6 angle. The Li-atom vibration in the $-c$ direction is limited only weakly by the three lower O ligands. It would be relatively easy for the Li nucleus to penetrate the large O_3 triangle with O···O vectors of 3.354 (2) [3.373 (2)] Å and thus move into the vacant interstice.

Table 4. *Atomic charges in electrons based on Hirshfeld partitioning of* $\Delta\rho$

$LiNbO_3$		$LiTaO_3$	
Atom	Charge	Atom	Charge
Li	−1.93 (8)	Li	−1.87 (13)
Nb	2.77 (9)	Ta	2.87 (30)
O	−0.28 (4)	O	−0.33 (21)

This possibility is reinforced by the Li-atom's vibration maximizing along the *c* direction.

5. Atomic charges

Atomic charges calculated by $\Delta\rho$ partitioning (Hirshfeld, 1977), listed in Table 4, are based on structure-factor models, including Zachariasen's (1967) extinction corrections. The $LiNbO_3$ charges are close to those for $LiTaO_3$, but differ from the formal values, as commonly observed for real charges measured by diffraction. The O-atom charge of –0.3 electrons is within the normal range for highly electronegative atoms in perovskites. If the Nb (Ta) charges in the structure were related to the asymmetry of interactions with the nearest-neighbour O ligands, the Ta charge would be less than that for the more strongly displaced Nb atom. This is not so. Approximately two electrons are transferred to the Li atom in both $LiNbO_3$ and $LiTaO_3$.

Conventional wisdom is that charges induced on cations such as Nb, Ta and Li will correspond in sign to the formal charge. Moving valence electrons from cations to anions completes the valence shells for anions. In the ionic model for bonding, an Li atom loses its one 2*s* electron, leaving an isotropic He-like wavefunction. It is difficult to identify experimental evidence to support the view that a bound Li cation's electron density resembles that of a free ion. An isotropic Li atom would be consistent with the wavefunction isotropy of the Li^+ free ion, but the structural geometry for the LiO_{12} moiety is strongly asymmetric. The Li-atom vibration is strongly anisotropic and its electron density is also asymmetric.

The hypothesis that exchange transfers electrons from tightly packed regions of a structure towards others that are packed less tightly (Maslen, Spadaccini, Ito, Marumo, Tanaka & Satow, 1993) explains why electrons accumulate near the Li atom, because it has the largest vibrations of all atoms in the structure. 'Exchange pressure' in $LiNbO_3$ and $LiTaO_3$ stabilizes additional electron density around the Li atom. The fact that three $Li\cdots B$ vectors are shorter than all $Li\cdots Li$ or $B\cdots B$ vectors, noted above, is readily explained if those atoms carry charges with opposite signs. The elongation of all Li—O vectors, with respect to the Li—O bond length of 2.000 Å in Li_2O (Wyckoff, 1963), is also consistent with repulsion between Li and O atoms carrying like charges.

6. Difference density

The reflection phases are only approximate because the structure is non-centrosymmetric. The $\Delta\rho$ map evaluated using the promolecule reference state contains only a component of the correct deformation density. Nevertheless, the degree of correspondence with those for related centrosymmetric structures (Buttner & Maslen, 1992) indicates that the more significant $\Delta\rho$ components provide a semi-quantitative picture of the factors responsible for ferroelectricity.

Spontaneous polarization in ferroelectric compounds must result from movement of electron density. The large charge movements in $LiNbO_3$ and $LiTaO_3$ are conveniently depicted in $\Delta\rho$ images of planes rotated by 7° from (01$\bar{1}$0), shown in Figs. 2 and 3,* that to a good approximation contain all types of *M*—O bonds. Electrons migrate towards the more loosely Li-occupied and vacant octahedra from tightly packed BO_6 groups

* $\sigma(\Delta\rho) = 0.31\ (0.60)$ e Å^{-3} (Cruickshank, 1949). Minimum $(\Delta\rho) = -2.7\ (-6.0)$ e Å^{-3}. Maximum $(\Delta\rho) = 3.5\ (3.4)$ e Å^{-3}.

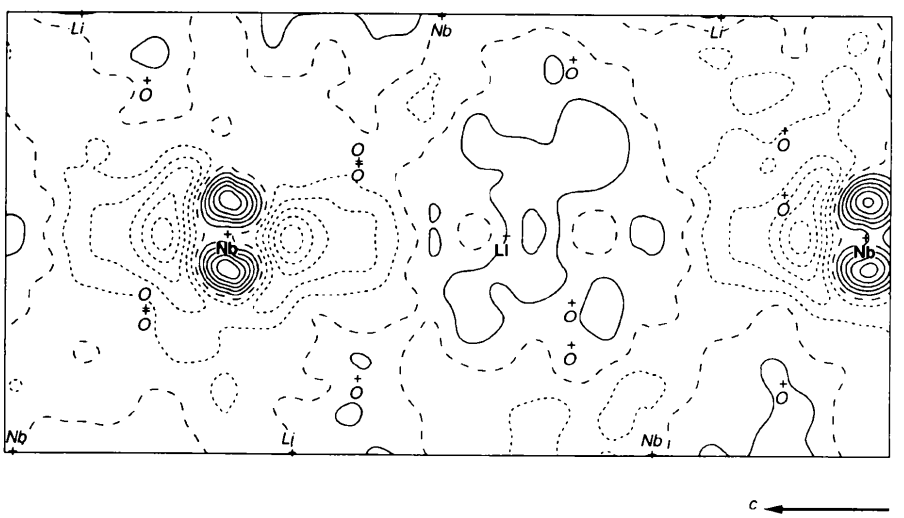

Fig. 2. $\Delta\rho$ for $LiNbO_3$ in a plane close to four distinct Li—O bonds and two Nb—O bonds. Map borders 9.6 × 4.8 Å. Contours: positive solid, negative dashes; interval 0.5 e Å^{-3}.

in both structures. The slowly varying $\Delta\rho$ around the Li nucleus, contrasting with sharper features around the Nb (Ta) nucleus, is consistent with the $_3$Li atom's small nuclear charge.

Electrons concentrate in a broad disc on the Li side of the nearest O_3 triangle. Excess $\Delta\rho$ extends from the Li nucleus through this large triangle into the vacant octahedron. This migration of electrons can be interpreted as the negative pole of an Nb(Ta)Li dipole, providing the basis for ferroelectricity. The structural geometry accounts elegantly for this $\Delta\rho$ topography. The $\Delta\rho$ topography suggests that the size of the O_3 triangles determines the broad characteristics of the electron density. Electrons migrate from the densely packed O_3 triangle between the BO_6 and LiO_6 groups towards the largest O_3 triangle. The Li atom's low nuclear charge implies that it would not be difficult for an Li atom to surmount a potential barrier aligned towards the double oxygen layers. The vibration amplitudes for Li along the c axis are correspondingly larger than those for the B atoms. The BO_6 octahedra are also more rigid.

The evidence that the Li atom's role in the ferroelectricity is crucial is persuasive. Low structural stability, indicated by the large Li-atom vibration parameters, explains its move into a symmetrical position in the paraelectric phase. Overlap of the Nb (Ta) atoms with its neighbours transfers electrons towards the Li atom, because it is loosely packed in the structure. The $\Delta\rho$ accumulation around the Li nucleus is mildly anisotropic. The refined atomic charge of -1.93 (-1.87) e for Li suggests involvement of both $2s$ and $2p$ states. A dipole component in the xy plane is precluded by symmetry. Three equivalent sp^2 hybrids maximizing at $2\pi/3$ generate a cylindrically symmetric function, although overlap of hybrid orbitals in a molecular orbital representation builds trigonally related $\Delta\rho$ peaks in Li—O bonds.

A sequence of distorted octahedra centred on Li,Nb(Ta) is intrinsically polar, irrespective of whether or not the Li and B atoms are at the centres of their respective octahedra. Complete non-polarity requires either that all atoms be neutral or that each B atom be symmetrically disposed within the BO_6 octahedron, with the Li atom disposed symmetrically about the face mid-point. This motif, with half a vacancy above and half below the Li atom, is the paraelectric structure. Assuming that the $\Delta\rho$ topography does not change drastically as the temperature rises, the Li nucleus would coincide with the centre of positive $\Delta\rho$ symmetry in the paraelectric structure. The $\Delta\rho$ gradients in Figs. 2 and 3 would generate a force attracting the Li nucleus towards the symmetrical position mid-way between the B atoms. Repulsive interaction with the closest O atoms would oppose the initial movement, but the Li—O interaction component along **c** vanishes at the metastable symmetrical position.

Hsu, Maslen & Ishizawa (1995) report depletion of $\Delta\rho$ along vectors between second nearest-neighbour heavy cations. In Figs. 2 and 3 the cation geometry matches the approximate $\Delta\rho$ symmetry, which the O atoms barely perturb. In this sense the charges, of both signs, in $LiNbO_3$ and $LiTaO_3$ should relate primarily to the cations. The shortest Li···B contact in the structure is the intercation vector between the nuclei in adjacent BO_6 and LiO_6 moieties. When these atoms overlap, the diatomic promolecule leads to a net repulsive force between the nuclei because of incomplete screening by the electrons, which is exacerbated by electron depletion along the cation–cation vector. It is opposed by the net repulsion of the cations overlapping with the nearby O atoms, as the B—O bond distances are shorter in the $+c$ direction for which the Li—O bonds are longer. Sharp features in the $\Delta\rho$ density close to the nuclei help to counterbalance any net force on the nuclei in the promolecule (Spackman & Maslen, 1985). Considering the atoms as distinct entities, Li and B attract because their charges have opposite signs. A decrease in the electron density along the line of the shortest Li···B

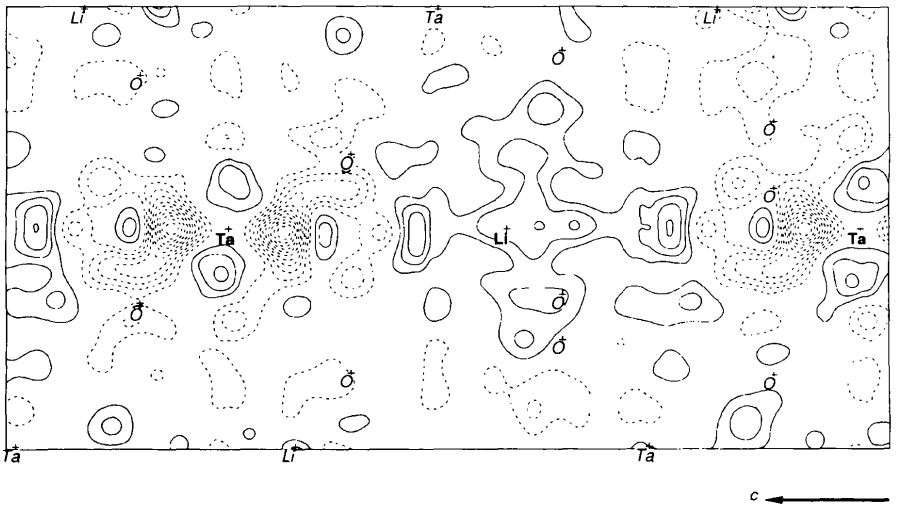

Fig. 3. $\Delta\rho$ for $LiTaO_3$ in a plane close to four distinct Li—O bonds and two Ta—O bonds. Map borders 9.6 × 4.8 Å. Contours: positive solid, negative dashes; interval 0.5 e Å^{-3}.

interaction, as occurs in Figs. 2 and 3, generates a counter-balancing repulsion.

The (0001) plane $\Delta\rho$ sections through Nb (Ta) atoms in Figs. 4 and 5 show $\bar{6}/m$ symmetry close to the metal. Mirror symmetry near the Ta atom is broken by the Li atoms displaced along **c**, which are not mirror-related. As the ground-state electron configuration for a neutral Ta atom is $[Xe]4f^{14}5d^36s^2$, *f*-type perturbations of the valence *s* and *d* electrons, which would generate states with odd values of *l*, cannot generate high even-order density multipoles of the type shown in Fig. 5. The $\Delta\rho$ topography cannot be explained by *f*-type perturbations of hybridized bound states. Extending the valence electron configuration to include unoccupied *f* orbitals for $LiTaO_3$ would introduce states with extended radial distributions and not the features with sixfold symmetry that occur near the Ta nucleus in Fig 5. The $\Delta\rho$ topography near the Nb (Ta) nucleus is consistent with the hypothesis that electron density is redistributed to a mild degree where tails of the valence distributions for neighbouring cations overlap with the closed inner subshells of the cations. Such electron redistribution accounts for high-order harmonics observed in the electron redistribution.

The $\Delta\rho$ maps near the *B* nuclei in Figs. 2 and 3 display quadrupolar t_{2g} pseudo-symmetry, as expected for π-bonding (Goodenough & Kafalas, 1973). The strong *c*-axis depletion contributes a cylindrically symmetric quadrupole. Although the two structure models refined for $LiTaO_3$ differed only at the 3*s* level of significance, by amounts that would be insignificant for less accurate data, $\Delta\rho$ features near the Ta nucleus for

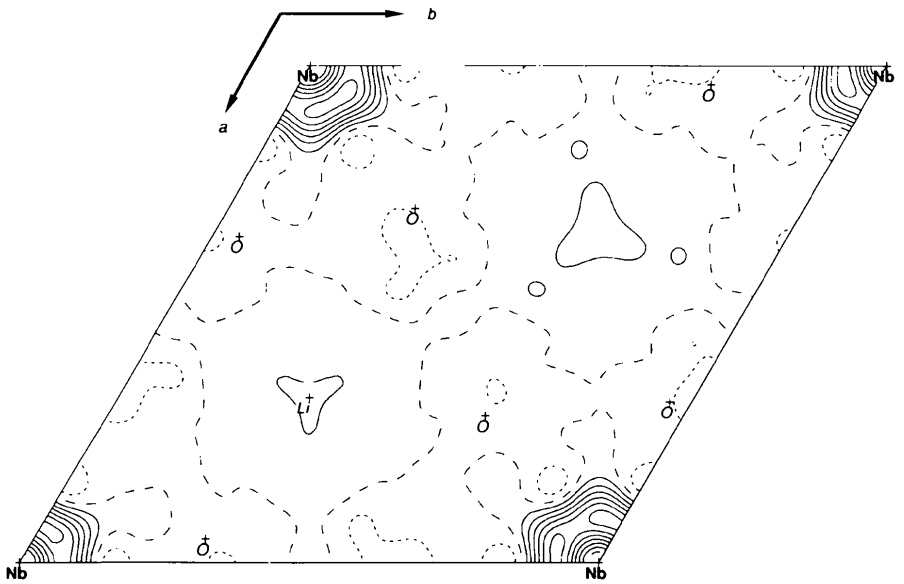

Fig. 4. $\Delta\rho$ containing Nb atoms in the (0001) plane of $LiNbO_3$. Map borders 5.148 × 5.148 Å. Contours: positive solid, negative dashes; interval 0.5 e Å^{-3}.

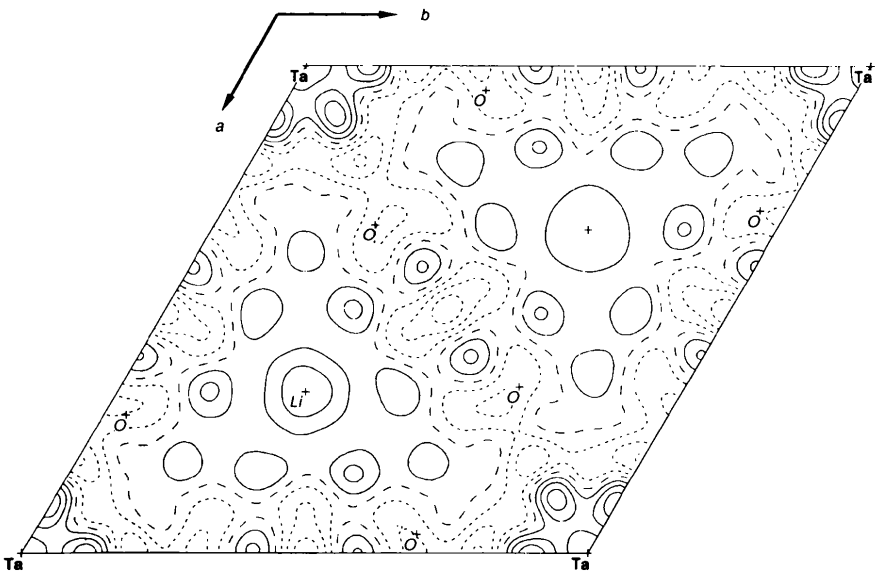

Fig. 5. $\Delta\rho$ containing Ta atoms in the (0001) plane of $LiTaO_3$. Map borders 5.154 × 5.154 Å. Contours: positive solid, negative dashes; interval 0.5 e Å^{-3}.

the two structures differed markedly, by removal of the obvious quadrupole in Fig. 3 from the structure with the higher R factor. This map had more obvious rapidly varying components, indicating the care needed when interpreting $\Delta\rho$ maps, even for structures with low R factors. Difference densities that contain no significant local quadrupole near the atom sites justify careful scrutiny.

We seek to understand the polar character of ferroelectric $LiNbO_3$ and its $LiTaO_3$ isomorph semi-quantitatively in terms of these synchrotron radiation images of structure and electron density. The spontaneous polarization $\mathbf{P}_s$, defined as twice the remanent polarization $\mathbf{P}_r$, represents the change in intrinsic polarization by reversing the applied field. The resulting factor of two is excluded when calculating spontaneous polarization in the present work.

Atomic charges are local averages of movements of electrons between atoms in a crystal. The distributed nature of the electron density raised a possible limitation of the charged atom model. The electric dipole moment $\mathbf{p}$ can be determined from a point-charge model or more rigorously by integrating partitioned difference density distribution. When $\mathbf{p}$ predicted by the two models did not differ significantly, the simpler point-charge model was accepted.

The Li- and B-atom displacements from the ferroelectric to the paraelectric phase are parallel. The short LiB direction determines the sense of the polar axis, with Li providing the negative pole and Nb (Ta) the positive pole. To eliminate polarity in $LiNbO_3$ ($LiTaO_3$) the B and Li cations must move 0.25 (4) [0.20 (1)] and 0.73 (1) [0.60 (2)] Å, respectively, along the c direction. The Hirshfeld charges for B and Li are 2.77 (2.87) and 1.93 (1.87) e, respectively. The dipole moments are calculated as (0, 0, +4.23) and (0, 0, +3.28) e for $LiNbO_3$ and $LiTaO_3$, respectively.

The dipole moment per unit volume is the polarization $\mathbf{P} = \mathbf{p}/V$ (Whitmer, 1962), where $\mathbf{p}$ is the dipole moment, e the elementary charge 1.6022×10^{-19} C and V the unit-cell volume, is $(3^{1/2}/4)a^2c$ for a hexagonal cell. Calculated spontaneous polarization of +0.43, +0.33 C m^{-2}, agrees semi-quantitatively with the experimentally measured values of +0.71, +0.50 C m^{-2} for $LiNbO_3$ and $LiTaO_3$, respectively (Abrahams & Keve, 1971). The relative ratio of 42.6/33.2 = 1.28 is close to the ratio 71/50 = 1.42 for the experimental measurements.

This work was funded by the IDP and Australian Research Council. Support from the Australian National Beamline Facility (ANBF), funded by a consortium comprising the ARC, DITARD, ANSTO, CSIRO, ANU and UNSW, is also acknowledged. It is a pleasure to thank Professor D. C. Creagh for his calculations of absorption coefficients and dispersion corrections, and Dr R. H. Buttner for his preparation of single-domain $LiNbO_3$ crystals.

References

Abrahams, S. C. (1994). *Acta Cryst.* A**50**, 658–685.
Abrahams, S. C. & Bernstein, J. L. (1967). *J. Phys. Chem. Solids*, **28**, 1685–1692.
Abrahams, S. C., Hamilton, W. C. & Reddy, J. M. (1966). *J. Phys. Chem. Solids*, **27**, 1013–1018.
Abrahams, S. C., Hamilton, W. C. & Sequeira, A. (1967). *J. Phys. Chem. Solids*, **28**, 1693–1698.
Abrahams, S. C. & Keve, E. T. (1971). *Ferroelectrics*, **2**, 129–154.
Abrahams, S. C., Levinstein, H. J. & Reddy, J. M. (1966). *J. Phys. Chem. Solids*, **27**, 1019–1026.
Abrahams, S. C. & Marsh, P. (1986). *Acta Cryst.* B**42**, 61–68.
Abrahams, S. C., Reddy, J. M. & Bernstein, J. L. (1966). *J. Phys. Chem. Solids*, **27**, 997–1012.
Alcock, N. W. (1974). *Acta Cryst.* A**30**, 332–335.
Boysen, H. & Altorfer, F. (1994). *Acta Cryst.* B**50**, 405–414.
Buttner, R. H. & Maslen, E. N. (1992). *Acta Cryst.* B**48**, 639–644.
Cochran, W. (1973). *The Dynamics of Atoms in Crystals*, p. 126. London: William Clowes & Sons.
Creagh, D. C. (1992). Personal communication.
Cruickshank, D. W. J. (1949). *Acta Cryst.* **2**, 65–82.
Goodenough, J. B. & Kafalas, J. A. (1973). *J. Solid State Chem.* **6**, 493–501.
Hall, S. R., Flack, H. D. & Stewart, J. M. (1992). Editors. *Xtal3.2 User's Guide and Reference Manual*. Universities of Western Australia, Australia, and Maryland, USA.
Hirshfeld, F. L. (1977). *Isr. J. Chem.* **16**, 198–201.
Hsu, R. M. (1995). PhD thesis. Department of Physics, University of Western Australia, Australia.
Hsu, R. M., Maslen, E. N. & Ishizawa, N. (1996). *Acta Cryst.* B**52**, 569–575.
Kittel, C. (1986). *Introduction to Solid State Physics*, 6th ed., pp. 373–374. New York: John Wiley.
Larson, A. C. (1970). *Crystallographic Computing*, edited by F. R. Ahmed, S. R. Hall & C. P. Huber, pp. 291–294. Copenhagen: Munksgaard.
Lines, M. E. (1969). *Phys. Rev.* **177**, 819–829.
Lines, M. E. & Glass, A. M. (1979). *Principles and Applications of Ferroelectrics and Related Materials*, pp. 24–58. Oxford: Clarendon Press.
Lipson, H. & Cochran, W. (1957). *The Determination of Crystal Structures*, pp. 302–307. London: G. Bell & Sons.
Maslen, E. N. & Spadaccini, N. (1993). *Acta Cryst.* A**49**, 661–667.
Maslen, E. N., Spadaccini, N., Ito, T., Marumo, F., Tanaka, K. & Satow, Y. (1993). *Acta Cryst.* B**49**, 632–636.
Megaw, H. D. (1954). *Acta Cryst.* **7**, 187–194.
Megaw, H. D. (1968). *Acta Cryst.* A**24**, 583–588.
Megaw, H. D. (1973). *Crystal Structures: A Working Approach*, pp. 226–241. Philadelphia: W. B. Saunders.
Ohgaki, M., Tanaka, K. & Marumo, F. (1989). *Mineral. J.* **14**, 373–382.
Ohgaki, M., Tanaka, K. & Marumo, F. (1992). *Mineral. J.* **16**, 150–160.
Prokhorov, A. M. & Kuz'minov, Yu S. (1990). *Physics and Chemistry of Crystalline Lithium Niobate*. Bristol: IOP.

Satow, Y. & Iitaka, Y. (1989). *Rev. Sci. Instrum.* **60**, 2390–2393.
Schomaker, V. & Trueblood, K. N. (1968). *Acta Cryst.* B**24**, 63–76.
Spackman, M. A. & Maslen, E. N. (1985). *Acta Cryst.* A**41**, 347–353.
Ståhl, K., Kvick, Å. & Abrahams, S. C. (1990). *Acta Cryst.* A**46**, 478–485.
Varghese, J. N. (1972). *RIGBY: Thermal Motion Analysis.* Department of Physics, University of Western Australia, Australia.
Whitmer, R. M. (1962). *Electromagnetics*, 2nd ed., p. 72. New York: Prentice-Hall.
Wyckoff, W. G. (1963). *Crystal Structure*, 2nd ed., Vol. 1, p. III.12. New York: Wiley-Interscience.
Zachariasen, W. H. (1967). *Acta Cryst.* A**23**, 558–564.